Progress In Electromagnetics Research, Vol. 166, 23–41, 2019

Reconstruction of Two-Dimensional Objects Buried into Three-Part Space with Locally Rough Interfaces via Distorted Born Iterative Method

Yasemin Altuncu*, Tulun Durukan, and Riza Erhan Akdogan

Abstract—In this paper, the reconstruction problem of inaccessible objects buried into a three-part space with locally rough interfaces is solved by Distorted Born Iterative Method (DBIM). DBIM requires the calculation of the background electric field and Green's function in every iteration step via the solution of the direct scattering problem. Here, they are calculated numerically by using the buried object approach (BOA) which is very useful in the solutions of the problems including stratified media with locally rough interfaces. Various numerical applications have been performed to demonstrate the applicability and efficiency of the method. The method was found to be very successful in reconstructing moderate contrast objects when they were buried in the middle space. In this case, the method works effectively even if the buried objects and interface roughnesses have complex geometric structures. Moreover, the multiplicity of buried objects has no negative effect on the reconstruction results. Nevertheless, the results of reconstruction deteriorate when objects are buried in the bottom space. However, the accuracies of them are still on an acceptable level in this situation.

1. INTRODUCTION

The reconstruction of the geometric and material properties of an inaccessible object is extremely important in terms of many real-life problems such as biomedical imaging, underground exploration, and remote sensing applications.

The general procedure to solve an inverse electromagnetic scattering problem is to measure the scattered field in an observation domain outside the object to be reconstructed, then using it in an inversion algorithm to determine the unknown properties of this object. Therefore, if there is a chance of going around the object to collect the scattered field data, the chance of success of the reconstruction will be high [1–9]. However, if the object is embedded in a layered media, there is no possibility to approach the object and measure the scattered field at any point around it. In this case, the scattered field can only be measured in the top space, so the available data will be insufficient [10–23]. It is clear that the situation will worsen as the number of layers increases. Furthermore, if the interfaces of the layers are not planar, the problem will become more complicated as it is necessary to consider the effects of this disturbance. For that reason, there is not much work on this issue, and in most of the work done the roughness level is assumed to be in low level [18–20]. In this study, we focus on the solution of an inverse scattering problem related to the dielectric objects with arbitrary shape and number, buried into three-part space with locally rough interfaces having arbitrary shape and amplitude.

The inverse scattering problems are called as ill-posed in the sense of Hadamard [24] because their solutions are not unique and the scattered field data not linearly related to the scatterer. The nonlinear relationship makes it difficult to find closed-form solutions for inverse scattering problems.

Received 22 July 2019, Accepted 15 September 2019, Scheduled 9 October 2019
* Corresponding author: Yasemin Altuncu (yaltuncu@ohu.edu.tr).
The authors are with the Electrical and Electronics Engineering Department, Nigde Omer Halisdemir University, Nigde, Turkey.

However, the problem can be linearized under certain conditions such as the conditions of Born and Rytov approximations [4]. Both of them require that the contrast between the buried bodies and the background is small. The iterative methods with regularizations are frequently preferred in cases where Born and Rytov conditions are not met [1–10, 25–33]. Among them, Born iterative method (BIM) [25], distorted Born iterative method (DBIM) [1–10, 25, 26], contrast source inversion method (CSIM) [22, 23, 27–31], and subspace optimization method (SOM) [32, 33] are the most widely used ones.

The main difference of this study from the existing ones in the literature is that it deals with a much more complicated problem geometrically. In most of the studies in the literature, objects to be identified reside in a homogeneous media [1–9, 25–33], layered media with planar interfaces [10–17] or under slightly rough surfaces [18–20]. In contrast, the present study deals with a rather complex problem of reconstructing 2D objects embedded in a three-part space with rough interfaces. While the objects can be buried in the middle or bottom space, the electric field measurements can only be made in the top-space in the discussed scenario. Because the interfaces are rough, the problem is substantially complex both mathematically and computationally. To solve this problem, distorted Born iterative method which requires to direct solution of background electric field and background Green's function in every iteration step is used in this work. Since the background is a layered space with rough interfaces, it is not possible to find analytical solutions for the background electric field and the background Green's function. In this work, they are computed numerically by using the buried object approach (BOA) [34]. In this approach, the ridges and pits of the interfaces are regarded as fictitious buried dielectric objects. Then, the background field and Green's function are obtained by solving the direct scattering problem related to these objects.

Although the assumption that the roughness is known previously and local is perceived as restricting the practical use of the proposed method, there are many real-life applications in which the proposed method can be applied directly, such as the detection of breast cancer tumors or historical remains in a mound or through-wall imaging. It is also possible to come across many studies in the literature where the roughness is small in amplitude and randomly varying [18–20]. The results of the proposed method can be compared with those of the studies if local roughnesses are chosen as too large in the x_1 direction, too small in amplitude, and have randomly varying geometry.

The rest of the paper is organized as follows. In Section 2, the general formulation for the direct and inverse solution of the problem is given. Here, the calculation method of the background electric field and the Green's function based on the BOA method in a three-part space with locally rough interfaces and DBIM based inverse problem solution procedure are given in detail. Various numerical examples are presented to demonstrate the applicability of the method in Section 3. In the numerical examples, the objects with moderate contrast are selected. Because of the constraints of being a Born approximation-based method, DBIM is not very effective in reconstructing high contrast objects. With the use of multiple-frequency approaches [2], hybrid-DBIM, or modified-DBIM methods [3, 33], the presented work can also be extended for higher-contrast objects. However, this is not within the scope of this study, and the focus of this study is to prove that the DBIM method can be used to reconstruct the objects embedded in a complex environment such as three-part space with rough interfaces. Some conclusions are given in Section 4. Also, the expressions of the Green function and the electric field in the case of plane wave illumination for the background composed of three-part space with a planar interface are given in the Appendices.

2. GENERAL FORMULATION

The geometry of the problem is illustrated in Fig. 1. Here, three mediums with different dielectric properties, stratified along x_2-axis are separated by locally rough interfaces denoted by Γ_1 and Γ_2. The relative permittivity and conductivity of the mediums from top to bottom are ϵ_{r_1}, σ_1, ϵ_{r_2}, σ_2, and ϵ_{r_3}, σ_3, respectively. The permeability of the whole space is μ_0, i.e., all media are filled by simple non-magnetic dielectric materials. As seen from Fig. 1, the interfaces are roughened around the $x_2 = d$ and $x_2 = -d$ planes and defined by the functions $f_1(x_1)$ and $f_2(x_1)$. A dielectric object with cross-section B in $x_1 - x_2$ plane (in general, the object does not need to be single) is embedded in the middle or bottom space. The geometry is illuminated by an electromagnetic wave source excited in the top medium. The problem

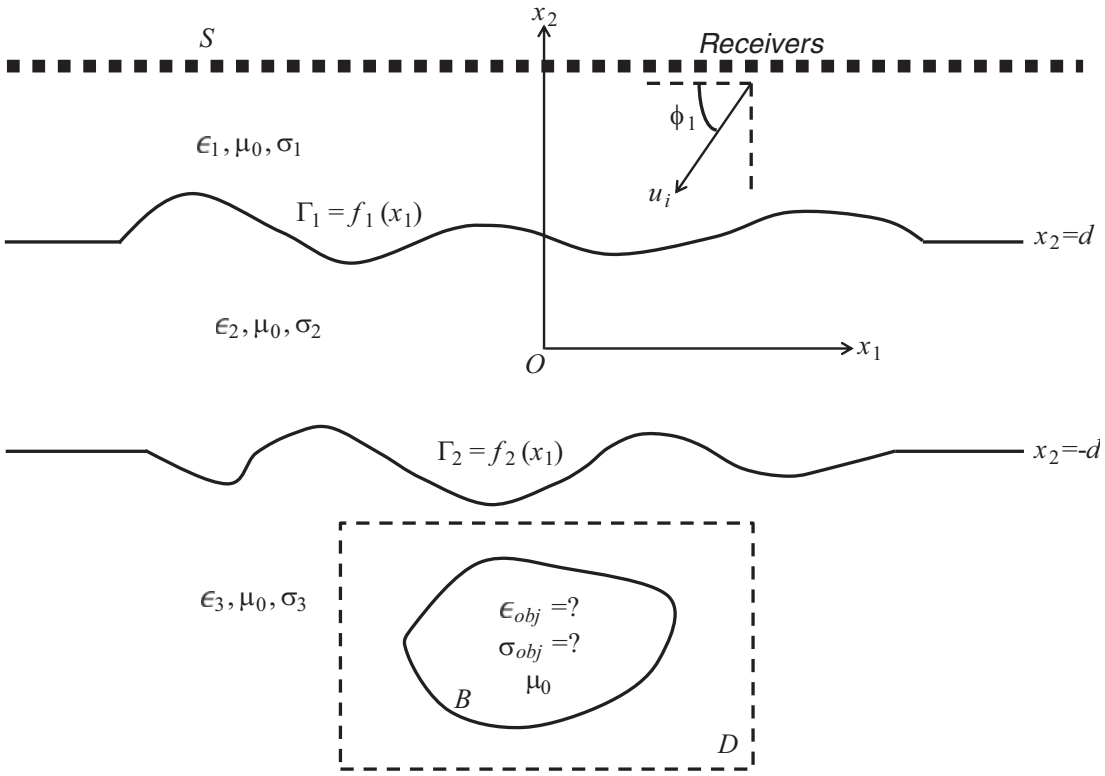

Figure 1. Geometry of the problem.

discussed in this work is to identify dielectric properties as well as the geometrical properties of the object located inside the domain of interest D by using the scattered field data measured in a domain S in the top medium. Here, D is called the reconstruction domain, and S is called the measurement domain. In this work, we deal with a two-dimensional case by assuming that the whole geometry is invariant along x_3-direction and illuminated by TM-polarized plane wave whose electric field is parallel to x_3-direction. It should be noted that even if line sources parallel to the x_3-direction are used instead of plane waves, the problem can also be reduced to a two-dimensional scalar problem.

It is important to know the nature and solution procedures of direct scattering problems to better understand the solutions of inverse scattering problems, Furthermore, most of the inverse scattering algorithm also requires the solution of the direct scattering problem in each iteration step, For that reason, in the following section, the solution method of the direct scattering problem is explained first.

2.1. Solution of the Direct Scattering Problem

The region of interest is illuminated by a TM-polarized plane wave whose electric field is supposed as parallel to the x_3-direction, i.e., $\mathbf{E}_i = (0, 0, u_i)$. The total electric field $\mathbf{E}$ at any point comprises the sum of the background field $\mathbf{E}_b$ and the scattered field $\mathbf{E}_s$. Since the geometry is invariant in x_3-direction and the incident field parallel to this direction, the background electric field and scattered electric field as well as the total electric field are also parallel to x_3-direction. That is $\mathbf{E}_b = (0, 0, u_b)$, $\mathbf{E}_s = (0, 0, u_s)$, and $\mathbf{E} = (0, 0, u)$. This allows us to reduce the problem to a scalar one and write the following scalar equation,

$$u = u_b + u_s \tag{1}$$

Here, the presence of the scattered field is due to the buried object, and this field satisfies the following integral equation including the background Green's function G_b,

$$u(\mathbf{x}) = u_b(\mathbf{x}) + \int_D k_b^2(y_2) G_b(\mathbf{x}, \mathbf{y}) \chi(\mathbf{y}) u(\mathbf{y}) d\mathbf{y} \tag{2}$$

where $\mathbf{x} = (x_1, x_2)$ is the position vector of a point in the measurement domain S, and $\mathbf{y} = (y_1, y_2)$ is the position vector of a point in reconstruction domain D. $k_b(y_2)$ is the wave number of the medium in which the domain D is located, and its explicit expression is as follows,

$$k_b(y_2) = \begin{cases} k_1, & y_2 \geq f_1(y_1) \\ k_2, & f_1(y_1) < y_2 < f_2(y_1) \\ k_3, & y_2 \leq f_1(y_1) \end{cases} \tag{3}$$

In Eq. (2), $\chi(\mathbf{y})$ is the object function that determines the contrast between the buried object and the background,

$$\chi(\mathbf{y}) = k^2(\mathbf{y})/k_b^2(y_2) - 1 \tag{4}$$

in which $k(\mathbf{y})$ is the value of the wave number at the point $\mathbf{y}$ in the reconstruction domain. It should be noted that $\chi(\mathbf{y})$ is zero if $\mathbf{y} \notin D$, because outside the D domain, $k(\mathbf{y}) = k_b(y_2)$.

The background field is equal to the total field in the absence of the scatterer. Since the background consists of a three-part space with locally rough interfaces, it is imperative to take into account the irregularities of the interfaces to calculate the background field and Green's function. The next section describes how the background field and background Green's function are calculated by the buried object approach (BOA) method.

Assume now that G_b and u_b are known. Then, one can solve the total field $u(\mathbf{y})$ at inner points of the domain of interest D by first dividing it into N rectangular cells, which are so small that u and χ are constant over a given cell. This allows us to write Eq. (2) in a matrix form as follows,

$$u(\mathbf{y}_m) = u_b(\mathbf{y}_m) + \sum_{n=1}^{N} k_b^2(y_2) G_b(\mathbf{y}_m, \mathbf{y}_n) \chi(\mathbf{y}_n) u(\mathbf{y}_n) \Delta s_n \tag{5}$$

where Δs_n is the cross-sectional area of nth cell while $m = 1, 2, \ldots, N$. Thus, the internal electric field in the domain D can be determined from the solution of the following system of linear equations,

$$[\mathbf{I} - \mathbf{A}]\mathbf{U} = \mathbf{U}_b \tag{6}$$

Here, $\mathbf{I}$ is the identity matrix with size $N \times N$, and $\mathbf{A}$ is a square matrix of the same size with entries defined by,

$$A_{mn} = k_b^2(y_2) G_b(\mathbf{y}_m, \mathbf{y}_n) \chi(\mathbf{y}_n) \Delta s_n \tag{7}$$

In Eq. (6), $\mathbf{U}$ and $\mathbf{U}_b$ are $N \times 1$ vectors whose entries are determined by $U_m = u(\mathbf{y}_m)$ and $U_{bm} = u_b(\mathbf{y}_m)$, $m = 1, 2, \ldots, N$. Once the internal electric fields are obtained in the domain of interest, the scattered field at any observation point $\mathbf{x}$ can be calculated as follows,

$$u_s(\mathbf{x}) = \sum_{n=1}^{N} k_b^2(y_2) G_b(\mathbf{x}, \mathbf{y}_n) \chi(\mathbf{y}_n) u(\mathbf{y}_n) \Delta s_n \tag{8}$$

2.2. Calculations of the Background Electric Field and Green's Function by BOA

According to the buried object approach (BOA), the roughnesses of the interfaces are considered as fictitious $2D$ buried bodies contouring by the $x_2 = f_1(x_1)$ function with $x_2 = d$ plane and $x_2 = f_2(x_1)$ function with $x_2 = -d$ plane as shown in Fig. 2. It is assumed that N_t objects whose electromagnetic parameters are the same as those of the middle space are buried in the top space, N_{mt} objects whose parameters are the same as those of the top space are buried in the middle space, N_{mb} objects whose parameters are the same as those of the bottom space are buried in middle space, and N_b objects whose parameters are the same as those of the middle space are buried in the bottom space. These objects are referred to as BOA objects. Thus, the problems of determining the background electric field and Green's function are reduced to the scattering problems of these fictitious objects in the case of plane wave illumination and point source illumination, respectively.

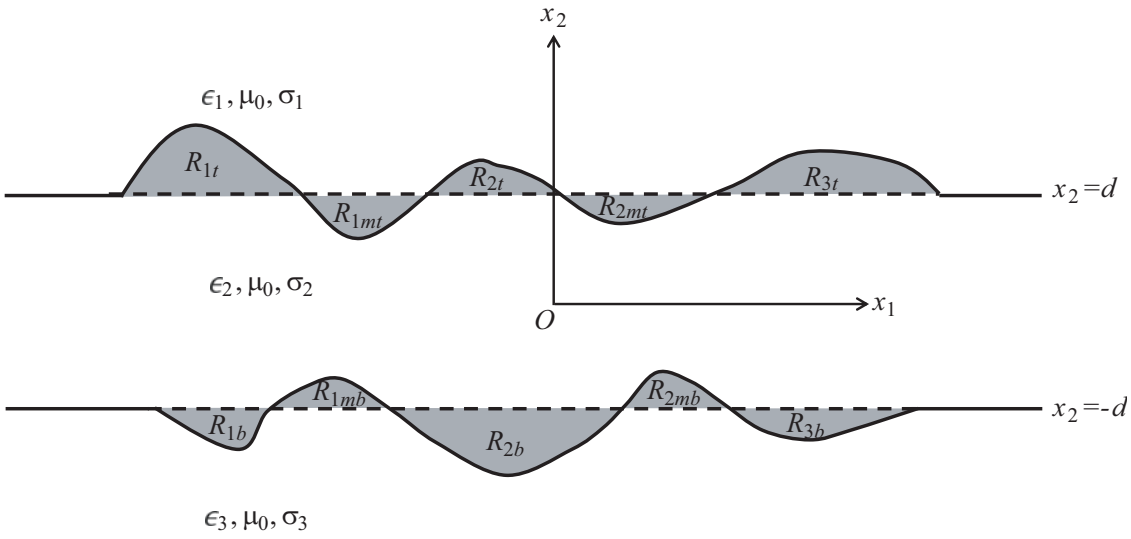

Figure 2. Buried object model of rough interfaces.

2.2.1. Background Field u_b

Let's suppose that the incident field is defined as follows,

$$u_i = e^{-ik_1(x_1\cos\phi_1 + x_2\sin\phi_1)} \tag{9}$$

where k_1 is the wave number of the top medium, and ϕ_1 is the incidence angle of the plane wave. Then, the background field can be expressed as,

$$u_b = u_{b0} + u_{sr} \tag{10}$$

where u_{b0} is the total field in three-part space separated by $x_2 = d$ and $x_2 = -d$ planes. This field can be easily calculated by using the reflection and transmission laws of plane waves from planar interfaces. Its explicit expression is given in Appendix A. u_{sr} is the field scattered by dielectric objects corresponding to the rough interfaces and satisfies the following integral equation,

$$\begin{aligned} u_b(\mathbf{x}) \;=\; & u_{b0}(\mathbf{x}) + k_1^2 \int\limits_{R_t} G_{b0}(\mathbf{x},\mathbf{z})\chi_{R_t}(\mathbf{z})u_b(\mathbf{z})d\mathbf{z} \\ & + k_2^2 \int\limits_{R_{mt}} G_{b0}(\mathbf{x},\mathbf{z})\chi_{R_{mt}}(\mathbf{z})u_b(\mathbf{z})d\mathbf{z} \\ & + k_2^2 \int\limits_{R_{mb}} G_{b0}(\mathbf{x},\mathbf{z})\chi_{R_{mb}}(\mathbf{z})u_b(\mathbf{z})d\mathbf{z} \\ & + k_3^2 \int\limits_{R_b} G_{b0}(\mathbf{x},\mathbf{z})\chi_{R_b}(\mathbf{z})u_b(\mathbf{z})d\mathbf{z} \end{aligned} \tag{11}$$

where $\mathbf{z} = (z_1, z_2)$ is the position vector of a point in the BOA objects, and $R_t = R_{1t} + R_{2t} + \ldots + R_{Nt}$, $R_{mt} = R_{1mt} + R_{2mt} + \ldots + R_{Nmt}$, $R_{mb} = R_{1mb} + R_{2mb} + \ldots + R_{Nmb}$, $R_b = R_{1b} + R_{2b} + \ldots + R_{Nb}$ are the cross-sectional areas of these objects. In Eq. (11), G_{b0} is the Green's function of the three-part space with planar interfaces whose explicit expression is given in Appendix B. $\chi_R(\mathbf{z})$ is the object function

related to the BOA objects,

$$\chi_R(\mathbf{z}) = \begin{cases} \chi_{R_t}(\mathbf{z}) = \dfrac{k_2}{k_1} - 1, & \mathbf{z} \in R_t \\ \chi_{R_{mt}}(\mathbf{z}) = \dfrac{k_1}{k_2} - 1, & \mathbf{z} \in R_{mt} \\ \chi_{R_{mb}}(\mathbf{z}) = \dfrac{k_3}{k_2} - 1, & \mathbf{z} \in R_{mb} \\ \chi_{R_b}(\mathbf{z}) = \dfrac{k_2}{k_3} - 1, & \mathbf{z} \in R_b \end{cases} \tag{12}$$

Denoting $R = R_t + R_{mt} + R_{mb} + R_b$, we can write Eq. (11) in a compact form as follows,

$$u_b(\mathbf{x}) = u_{b0}(\mathbf{x}) + \int_R k_{b0}^2(z_2) G_{b0}(\mathbf{x}, \mathbf{z}) \chi_R(\mathbf{z}) u_b(\mathbf{z}) d\mathbf{z} \tag{13}$$

where

$$k_{b0}^2(z_2) = \begin{cases} k_1^2, & z_2 >= d \\ k_2^2, & -d <= z_2 < d \\ k_3^2, & z_2 < -d \end{cases} \tag{14}$$

Here, u_{sr} and u_b are calculated numerically, similar to u_s and u in Section 2.1.

2.2.2. Background Green's Function G_b

Unlike the calculation of the background electric field, the point source is used for the calculation of the background Green's function. So, the Green's function requires the solution of the following integral equation,

$$G_b(\mathbf{x}, \mathbf{y}) = G_{b0}(\mathbf{x}, \mathbf{y}) + \int_{R_u} k_{b0}^2(z_2) G_{b0}(\mathbf{x}, \mathbf{z}) \chi_R(\mathbf{z}) G_b(\mathbf{z}, \mathbf{y}) d\mathbf{z} \tag{15}$$

Here again, the solution of this integral equation is obtained numerically.

2.3. Solution of the Inverse Scattering Problem

The geometry of interest is successively illuminated by plane waves defined in Eq. (9) with incremental incidence angles indicated by ϕ_1^p, $p = 1, 2, \ldots, P$. Then, the scattered fields are measured on a domain composed of M points along a straight line in the top layer. This measurement domain is denoted by S in Fig. 1. The object function given in Eq. (4) is to be reconstructed by solving inverse scattering problem. It should be noted that Eq. (2) forms a nonlinear integral equation because $u(\mathbf{y})$ depends on $\chi(\mathbf{y})$. In this work, Distorted Born Iterative Method (DBIM) is used to reconstruct the unknown object function distribution throughout the reconstruction domain D.

The first step of DBIM is to use the Born approximation to obtain an initial guess for object function. According to Born approximation, the total field in the reconstruction domain can be approximated as background field, i.e., $u(\mathbf{y}) = u_b(\mathbf{y})$ in the integral given in Eq. (2) to linearize the equation. In the next description, superscript i indicates the iteration step. So, for any incidence angle ϕ_1^p, we need to solve the following integral equation to obtain the zeroth-order object function $\chi^{i=0,p}$, i.e., initial guess,

$$u_s^p(\mathbf{x}) = \int_D k_b^2(y_2) G_b(\mathbf{x}, \mathbf{y}) \chi^{0,p}(\mathbf{y}) u_b^p(\mathbf{y}) d\mathbf{y} \tag{16}$$

This integral can be represented in matrix form by discretizing the domain,

$$\mathbf{U}_s^p = \mathbf{Q}^p \mathbf{X}^{0,p} \tag{17}$$

Here, $\mathbf{Q}^p$ is an $M \times N$ size inverse scattering matrix with entries,

$$Q^p_{mn} = k_b^2(y_2) G_b(\mathbf{x}_m, \mathbf{y}_n) u_b^p(\mathbf{y}_n) \Delta s_n \tag{18}$$

$\mathbf{U}_s^p$ is an $M \times 1$ vector with entries $U^p_{sm} = u_s^p(\mathbf{x}_m)$, $m = 1, 2, \ldots, M$. It is composed of measured scattered field data for incidence angle ϕ_1^p. $\mathbf{X}^{0,p}$ is an $N \times 1$ vector with entries unknown zeroth-order object function at points of reconstruction domain for incidence angle ϕ_1^p. The entries of this vector are defined by $X_n^{0,p} = \chi^{0,p}(\mathbf{y}_n), n = 1, 2, \ldots, N$. Due to the ill-posed nature of Eq. (16), it is not possible to find $\mathbf{X}$ directly from the product of the inverse of the matrix $\mathbf{Q}$ and the scattered field data vector $\mathbf{U}_s$. In this work, Tikhonov regularization [35, 36] is applied to overcome this handicap, and the object function distribution at any iteration step and incidence angle is obtained by following matrix calculation,

$$\mathbf{X} = [\mathbf{Q}^* \mathbf{Q} + \gamma \mathbf{I}]^{-1} [\mathbf{Q}^* \mathbf{U}_s] \tag{19}$$

where $\mathbf{I}$ is an $N \times N$ identity matrix; γ is the regularization parameter; and asterisk refers to complex conjugate. Since Tikhonov regularization is applied in each iteration step, superscripts denoting iteration number and incidence angle are not shown in this expression for the sake of generalization. After the object function is calculated for all incidence angles, the zeroth-order object function is derived from their mean value as follows

$$\mathbf{X}^0 = \frac{1}{P} \sum_{p=1}^{P} \mathbf{X}^{0,p} \tag{20}$$

Distorted Born iteration starts from this point. The updated quantities are indicated with a bar. The zeroth-order object function calculated before is used in the integral equation of the direct problem in Eq. (5) to calculate the inner fields in the reconstruction domain. Accordingly, $\bar{u}^{i,p}(\mathbf{y})$ is updated as follows,

$$\bar{\mathbf{U}}^{i,p} = [\mathbf{I} - \mathbf{A}^i]^{-1} \mathbf{U}_b^p \tag{21}$$

where $\bar{\mathbf{U}}^{i,p}$ is an $N \times 1$ vector whose entries are composed of the total field at discretized points of reconstruction domain for the pth incidence angle at the ith iteration step. $\mathbf{A}^i$ is a square matrix whose entries are defined by,

$$A^i_{mn} = k_b^2(y_2) G_b(\mathbf{x}_m, \mathbf{y}_n) \chi^{i-1}(\mathbf{y}_n) \Delta s_n \tag{22}$$

The next step of the DBIM algorithm is to update the background Green's function. Since the background Green's function is the point source response of the background medium, it can be calculated in the same way as the background electric field, except that the point source excitation is used instead of plane wave excitation. So, the response of point sources on the measurement domain at the points in the reconstruction domain is

$$\bar{G}_b^i(\mathbf{y}, \mathbf{x}) = (\mathbf{I} - \mathbf{A}^i)^{-1} G_b^T(\mathbf{x}, \mathbf{y}) \tag{23}$$

where superscript T indicates the transpose. Then, the desired background Green's function at the ith step is $\bar{G}_b^i(\mathbf{x}, \mathbf{y}) = \bar{G}_b^{iT}(\mathbf{y}, \mathbf{x})$.

In the subsequent step, the scattered field on the measurement domain is computed using the last reconstructed object function, background Green's function, and the background electric field in Eq. (2),

$$\bar{u}_s^{i,p}(\mathbf{x}) = \int_D k_b^2(y_2) \bar{G}_b^i(\mathbf{x}, \mathbf{y}) \chi^i(\mathbf{y}) \bar{u}^{i,p}(\mathbf{y}) d\mathbf{y}. \tag{24}$$

A deviation of the measured scattered field u_s from the ones calculated in the ith iteration step is denoted by $\Delta u_s(\mathbf{x})$ that is equal to the difference between measured and calculated scattered fields,

$$\begin{aligned} \Delta u_s^{i,p}(\mathbf{x}) &= u_s^p(\mathbf{x}) - \bar{u}_s^{i,p}(\mathbf{x}) \\ &= \int_D k_b^2(y_2) \bar{G}_b^i(\mathbf{x}, \mathbf{y}) \Delta \chi^{i,p}(\mathbf{y}) \bar{u}^{i,p}(\mathbf{y}) d\mathbf{y}. \end{aligned} \tag{25}$$

This equation can be written in matrix form,

$$\Delta \mathbf{U}_s^{i,p} = \mathbf{U}_s^p - \bar{\mathbf{U}}_s^{i,p} = \mathbf{Q}^{i,p} \Delta \mathbf{X}^{i,p}. \tag{26}$$

Here, $\mathbf{U}_s^p$ and $\bar{\mathbf{U}}_s^{i,p}$ are $M \times 1$ vectors denoting the measured and the calculated scattered field vectors, respectively, and $\Delta\mathbf{U}_s^{i,p}$ is difference scattered field vector. $\mathbf{Q}^{i,p}$ is an $M \times N$ matrix, and the difference from Eq. (21) is that it uses $\bar{G}_b^i$ instead of G_b and $\bar{u}^{i,p}$ instead of u_b^p in the entries, i.e.,

$$Q_{mn}^{i,p} = k_b^2(y_2)\bar{G}_b(\mathbf{x}_m, \mathbf{y}_n)\bar{u}^{i,p}(\mathbf{y})\Delta s_n \tag{27}$$

It should be noted that the updated Green's function $\bar{G}_b^i$ is used only in the calculated scattered field expressions from Eqs. (24) to (26). The Green's function G_b shown in Eqs. (22) and (23) is the initially known Green's function of the background. Tikhonov regularization procedure is employed here to obtain $\Delta\mathbf{X}^{i,p}$. $\Delta\mathbf{X}^i$ is the difference object function vector measured between two consecutive iteration steps, and it is calculated by,

$$\Delta\mathbf{X}^i = \frac{1}{P}\sum_{p=1}^{P}\Delta\mathbf{X}^{i,p}. \tag{28}$$

for $p = 1, 2, \ldots, P$. Then, the object function is updated as,

$$\mathbf{X}^{i+1} = \mathbf{X}^i + \Delta\mathbf{X}^i \tag{29}$$

Iteration is continued until the relative residual error (RRE) reaches a predetermined criterion. RRE is defined as,

$$RRE = \frac{\sum_{m=1}^{M}\sum_{p=1}^{P}|U_{sm}^p - \bar{U}_{sm}^{i,p}|^2}{\sum_{m=1}^{M}\sum_{p=1}^{P}|U_{sm}^p|^2} \tag{30}$$

It should be reminded that here m indicates the mth measurement point, and p indicates the pth incidence angle.

3. NUMERICAL RESULTS

In this section, some reconstruction results of dielectric objects buried into the middle or bottom medium of three-part space are presented. In all examples, the top space is considered as free-space, i.e., $\epsilon_1 = \epsilon_0, \mu_1 = \mu_0$. Furthermore, the frequency is considered as 300 MHz, and all dimensions are given in the wavelength of free-space, λ. In all the examples, Tikhonov regularization parameter is selected between 10^{-14} and 10^{-10}. As the noise level, the conductivity of the middle and bottom spaces, the roughness size, and the dimensions of the region of interest increase, it is appropriate to select the regularization parameter larger. If this parameter is selected too small, it does not regularize the solution, and if it is selected too large, it smoothes the solution too much. The measured scattered field data are generated synthetically by solving forward problem using moments method, and 5% Gaussian white noise $ns = \eta|u_s|W$ is added to data. Here, η is the noise level, and W is a complex vector whose real and imaginary parts are composed of normally distributed random numbers with zero mean. Then, the corresponding signal to noise ratio in decibel is obtained by $SNR_{\text{dB}} = 10\log_{10}\frac{\sum_{m=0}^{M}|u_s(m)|}{\sum_{m=0}^{M}|ns(m)|}$.

The first example is devoted to revealing the effect of the medium in which the objects are buried in the success of the reconstruction. To see this effect, the reconstruction results of the same objects when they are buried in the middle and bottom spaces are compared. Here, the constitutive parameters of the middle-space are $\epsilon_{r2} = 1.3, \sigma_2 = 10^{-6}$, while those of bottom space are $\epsilon_{r3} = 1.5, \sigma_3 = 10^{-4}$. The thickness of the middle space is $2d = 2.2\lambda$. Thus, with reference to Fig. 1 the top and middle spaces are separated from each other by a rough interface fluctuating around the center line $x_2 = d = 1.1\lambda$ with the middle and bottom spaces by a rough interface fluctuating around the center line $x_2 = -d = -1.1\lambda$. The roughness of the interface dividing top and middle spaces is considered as a randomly rough surface specified by correlation length 0.4λ, rms height 0.2λ, and roughness length 20λ. Similarly, the roughness of the interface dividing the middle and bottom space is also considered as a random surface specified by the same correlation length and rms height with upper interface roughness, but this time the roughness

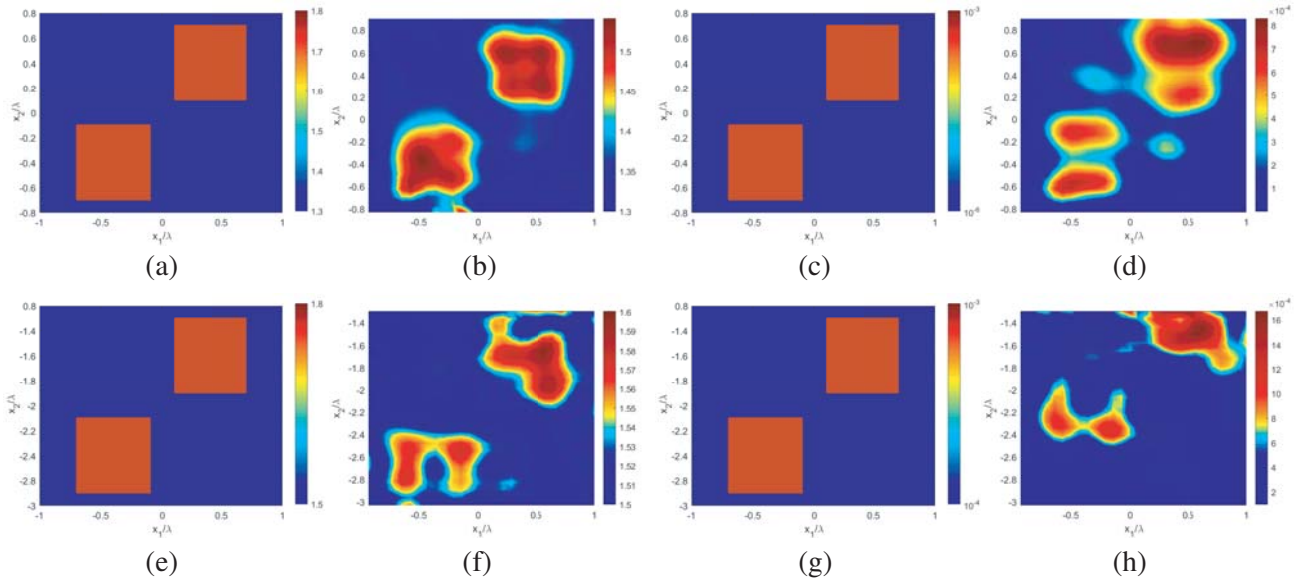

Figure 3. Reconstruction results of two square-shaped objects with parameters $\epsilon_{obj} = 1.7, \sigma_{obj} = 0.001$ buried in middle and bottom spaces. (a) Original permittivity-middle space. (b) Reconstructed permittivity-middle space. (c) Original conductivity-middle space. (d) Reconstructed conductivity-middle space. (e) Original permittivity-bottom space. (f) Reconstructed permittivity-middle space. (g) Original conductivity-bottom space. (h) Reconstructed conductivity-bottom space.

length is 10λ. In the first scenario, two identical rectangular-shaped objects with dimensions $0.6\lambda \times 0.6\lambda$ are embedded in the middle space such that their center points are $(-0.4\lambda, -0.4\lambda)$ and $(0.4\lambda, 0.4\lambda)$. In the second scenario, the same objects are embedded in the bottom space. The center points of the objects are $(-0.4\lambda, -2.4\lambda)$ and $(0.4\lambda, -1.6\lambda)$ at this time. The relative permittivity and the conductivity of both objects are $\epsilon_{obj} = 1.7, \sigma_{obj} = 0.001$. The measurement domain S is selected as 50λ straight line above the top rough interface at $x_2 = 1.3\lambda$ in the top space. The electric fields are observed at 100 points along the measurement domain as the geometry of interest is illuminated by plane waves with 30 different incidence angles in $\phi_1 \in (-\pi/2, \pi/2)$, successively. A $2\lambda \times 1.8\lambda$ rectangular reconstruction domain is considered and meshed to 28×26 pixels. The original and reconstructed relative permittivity distributions are given in Figs. 3(a) and 3(b) when the objects are buried in the middle space. Besides, in Figs. 3(c) and 3(d), the original and reconstructed conductivities are given for the same scenario. On the other hand, the original and reconstructed relative permittivities are given in Figs. 3(e) and 3(f) when these two square-shaped objects are buried in the bottom space. Finally, the original and reconstructed conductivity distributions are given in Figs. 3(g) and 3(h) for the second scenario.

The comparison of relative residual error (RRE) graphics obtained for the cases where the objects are in the middle and bottom spaces is given in Fig. 4. As expected, the results obtained for the first scenario are better than those for the second scenario. Nevertheless, the reconstruction results are also satisfactory for the last case.

In the last phase of the first example, a larger reconstruction domain is selected to observe its effects on the reconstruction result. While in the previous configuration the region of interest, i.e., the reconstruction domain is $2\lambda \times 1.8\lambda$, this time it is $2.5\lambda \times 2.5\lambda$. Figs. 5(a) and 5(b) show the reconstructed relative permittivity and conductivity along the region of interest which resides in middle space. Besides, Figs. 5(c) and 5(d) show the results of reconstruction when the region of interest is in the bottom space. The comparison of Fig. 3 and Fig. 5 shows that when the domain is small, the reconstruction results are more successful in both value and geometry than in the case where it is larger. However, when the domain is small, unexpected strong values appear where objects approach the boundaries of the domain.

The second example aims to show that objects with extraordinary geometrical shapes and inhomogeneous constitutive parameters can be reconstructed with the presented method. For that

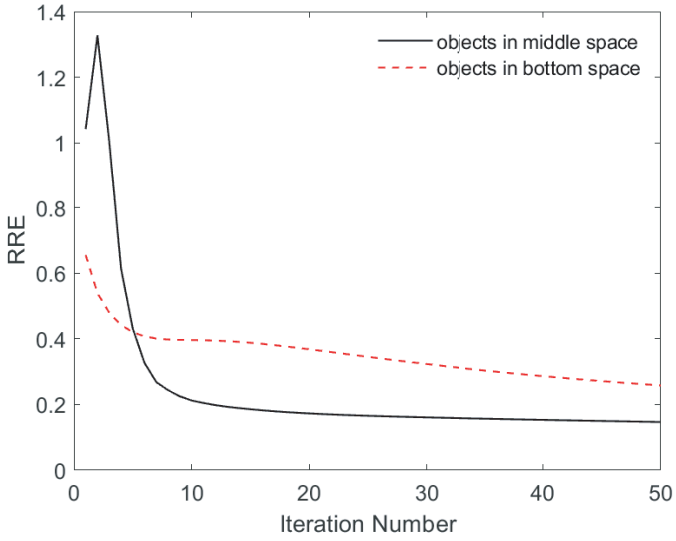

Figure 4. Relative residual error for reconstruction of buried two square-shaped objects.

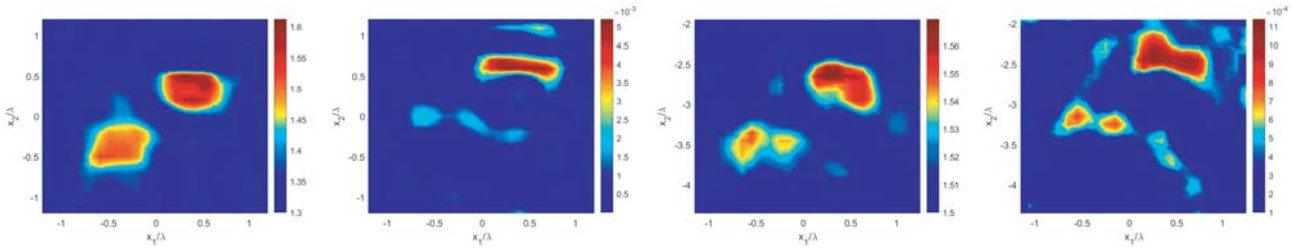

Figure 5. Reconstruction results of two square-shaped objects with an enlarged domain of interest in middle and bottom spaces. (a) Reconstructed permittivity-middle space. (b) Reconstructed conductivity-middle space. (c) Reconstructed permittivity-bottom space. (d) Reconstructed conductivity-bottom space.

purpose, first, an inhomogeneous object shown in Fig. 6(a), which is placed into middle space, is considered. Here, the first part of the object is a hollow disc with radius 0.5λ and center $(0, 0)$. The radius of the hole is 0.2λ, and center is $(0.1\lambda, 0.2\lambda)$. Another part of the object is a solid disc with a radius of 0.2λ at the center $(0.3\lambda, 0.5\lambda)$. The dimensions of the reconstruction domain are considered as $1.8\lambda \times 1.8\lambda$. The constitutive parameters of the hollow disc are $\epsilon_{obj} = 1.7, \sigma_{obj} = 0.001$ while those of the solid disc are $\epsilon_{obj} = 1.8, \sigma_{obj} = 0.01$. The constitutive parameters of the three-part space and the roughness of the interfaces are considered the same as the first example. From the reconstructed relative permittivity distribution throughout the reconstruction domain in Fig. 6(b), the geometries and relative permittivity values of the objects can be distinguished. Also, the original and reconstructed conductivities of the object are shown in Figs. 6(c) and 6(d), respectively. Secondly, a sawtooth-shaped homogeneous object with dielectric permittivity $\epsilon_{obj} = 1.7, \sigma_{obj} = 0.001$ buried into the same medium is reconstructed. Here again, the reconstruction results are extremely successful although the subject has sharp edges, as shown from Figs. 7(a) to 7(d). In the last step of this example, an object similar to a square-wave shape that has the same electromagnetic parameters as the previous object is considered. The method is very successful again in reconstructing the objects with these different geometries as shown in Figs. 8(a) to 8(d).

In the third example, the effect of the roughness size on reconstruction performance is investigated.

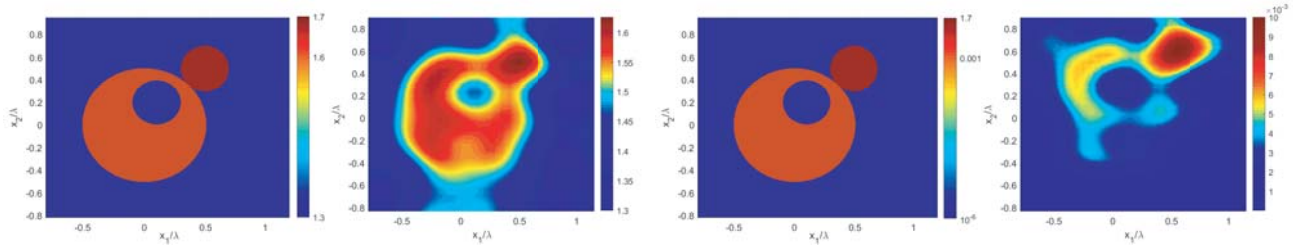

(a) (b) (c) (d)

Figure 6. Reconstruction results of an inhomogeneous annular disc-shaped objects. (a) Original permittivity. (b) Reconstructed permittivity. (c) Original conductivity. (d) Reconstructed conductivity.

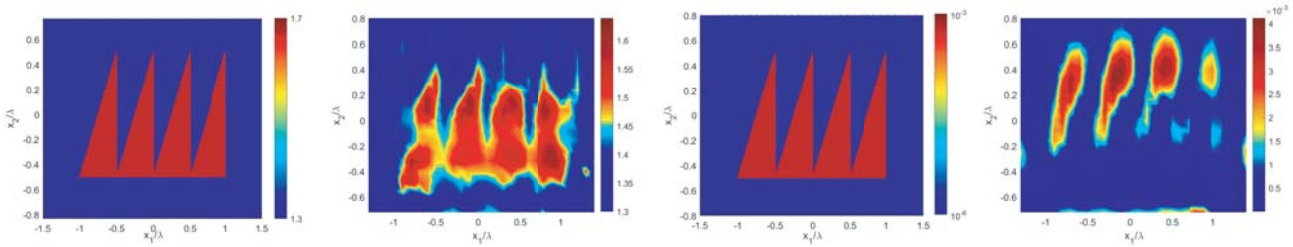

(a) (b) (c) (d)

Figure 7. Reconstruction results sawtooth-shaped object with parameters $\epsilon_{obj} = 1.7, \sigma_{obj} = 0.001$. (a) Original permittivity. (b) Reconstructed permittivity. (c) Original conductivity. (d) Reconstructed conductivity.

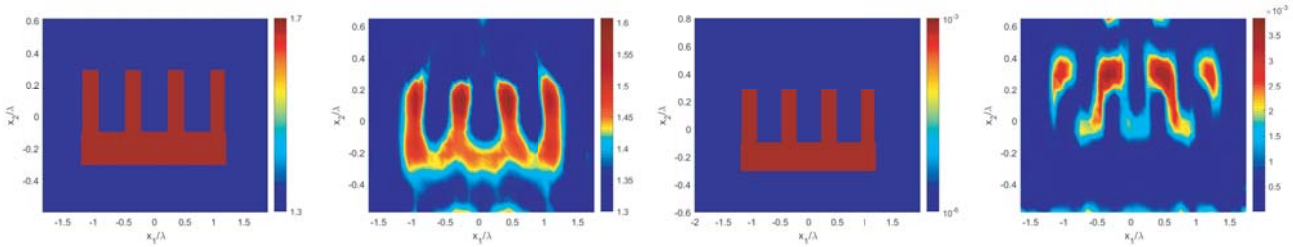

(a) (b) (c) (d)

Figure 8. Reconstruction results square-wave shaped object with parameters $\epsilon_{obj} = 1.7, \sigma_{obj} = 0.001$. (a) Original permittivity. (b) Reconstructed permittivity. (c) Original conductivity. (d) Reconstructed conductivity.

In order to observe this effect more explicitly, both roughnesses are chosen as sinusoidal defined by the function $f(x) = \alpha \sin \frac{2\pi x}{4}$. Here α determines the amplitude of the roughness. An "Austria profile" object is placed in the middle space with the center of the ring $(0, -0.15\lambda)$. The relative permittivity and conductivity of the objects are equal to $\epsilon_{obj} = 1.8$ and $\sigma_{obj} = 0.01$. The thickness of the middle space is $2d = 2.4\lambda$, and the length of local roughness for both interfaces is 16λ. In each case in this example, the scattered fields are measured at 100 points along a 50λ length line 0.1λ above the top roughness. Here, the amplitude of sinusoidal roughness α is changed from 0 (planar interface) to 0.4λ (peak to peak 0.8λ) gradually for both interfaces, and their effects on reconstruction are observed. In Figs. 9(a) and 9(b), the reconstructed permittivity and conductivity distributions are given when the interfaces dividing the three-part space are planar. Figs. 9(c) and 9(d) show the reconstructed permittivity and conductivity distributions when amplitudes of the roughnesses for both interfaces are equal to 0.1λ while in Figs. 9(e) and 9(f), $\alpha = 0.3\lambda$. Finally, in the last two figures, Figs. 9(g) and 9(h), the reconstructed permittivity and conductivity distributions are given for $\alpha = 0.4\lambda$. It can be noted

that the roughness sizes are in the same order with the reconstructed object dimensions when $\alpha = 0.2\lambda$ while they are bigger than object dimensions when $\alpha = 0.4\lambda$. As expected, as the amplitude of the roughness increases, the reconstruction results are deteriorated because the impact of the roughness on the total field becomes dominant. This creates a noise-like effect on the data to be used in the solution of the inverse scattering problem and negatively affects the results of the reconstruction. In Fig. 10, RRE is plotted versus iteration number for different values of the roughness amplitude.

In the last example, firstly, 10 circular objects with a radius of 0.15λ are reconstructed by the proposed method. The roughness shapes of the interfaces of three-part space are the same as the first example. However, the thickness of the middle space is 2.6λ at this time. To better model real

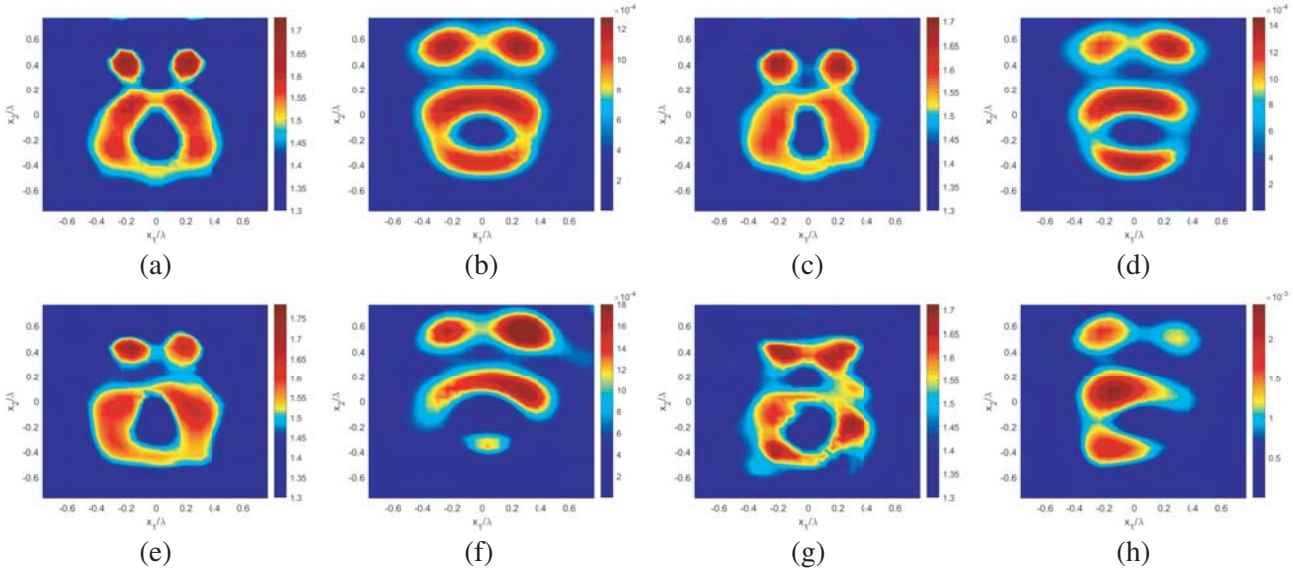

Figure 9. Reconstruction results of Austria profile object with parameters $\epsilon_{obj} = 1.8$ and $\sigma_{obj} = 0.01$. (a) Reconstructed permittivity for planar interfaces. (b) Reconstructed conductivity for planar interfaces. (c) Reconstructed permittivity for $\alpha = 0.1\lambda$. (d) Reconstructed conductivity for $\alpha = 0.1\lambda$. (e) Reconstructed permittivity for $\alpha = 0.3\lambda$. (f) Reconstructed conductivity for $\alpha = 0.3\lambda$. (g) Reconstructed permittivity for $\alpha = 0.4\lambda$. (h) Reconstructed conductivity for $\alpha = 0.4\lambda$.

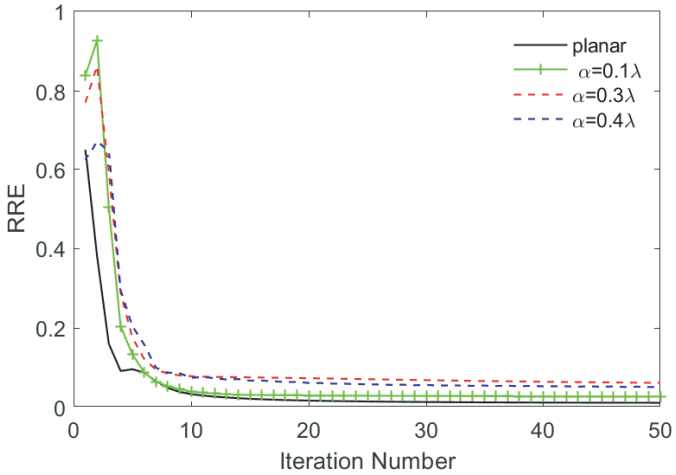

Figure 10. Relative residual error for reconstruction of Austria profile object buried between rough interfaces of various amplitudes.

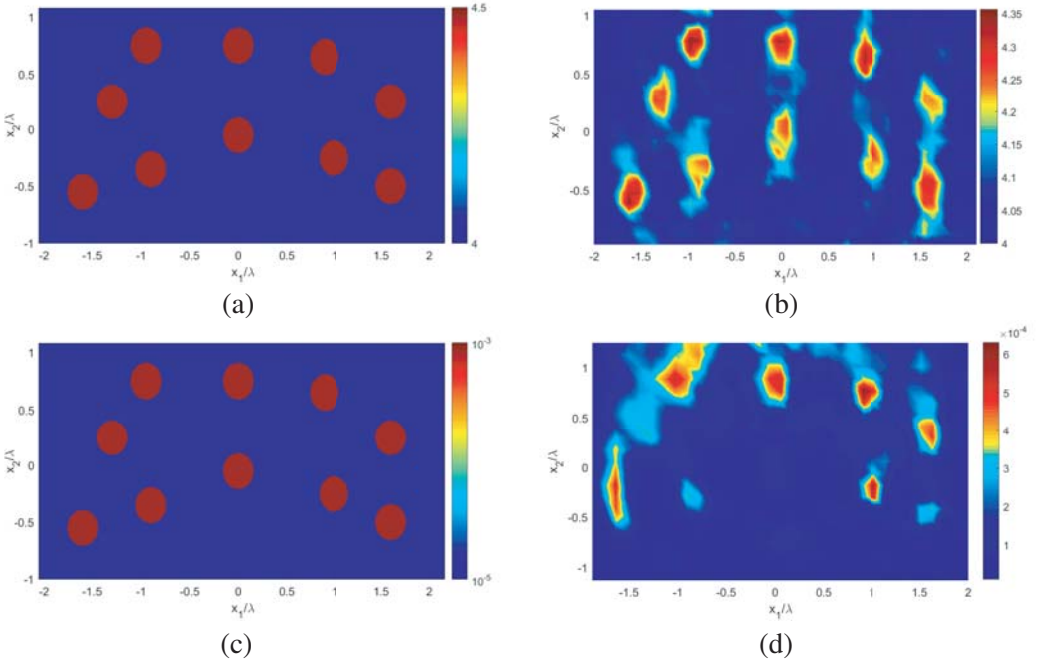

Figure 11. Reconstruction results of 10 identical circular objects with parameters $\epsilon_{obj} = 4.5$ and $\sigma_{obj} = 0.001$. (a) Original permittivity. (b) Reconstructed permittivity. (c) Original conductivity. (d) Reconstructed conductivity.

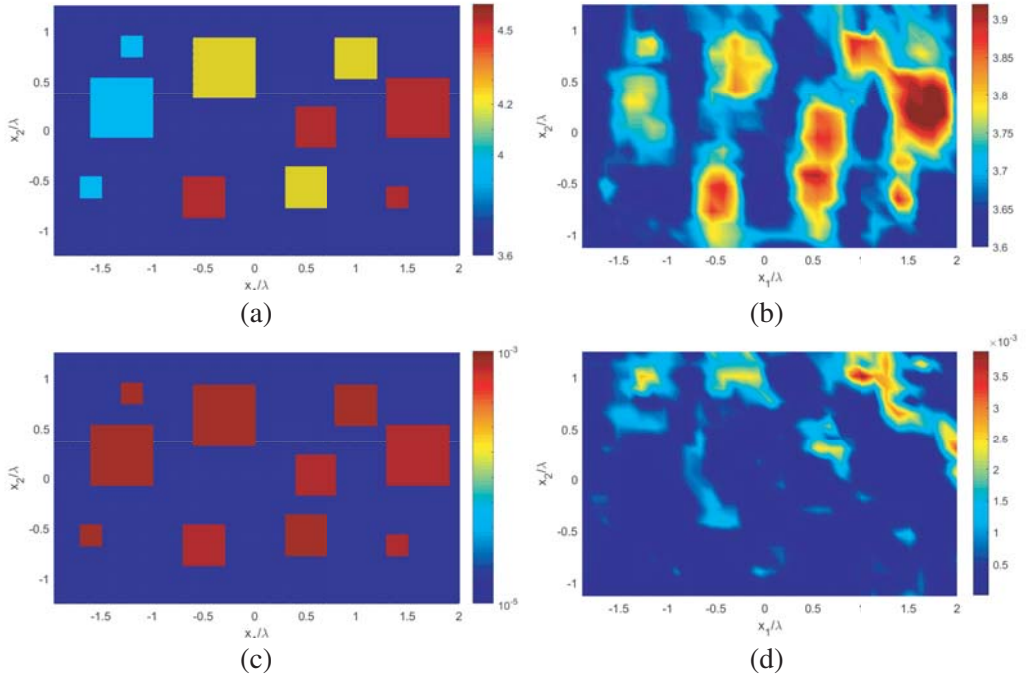

Figure 12. Reconstruction results of 10 square objects with different size and permittivity. (a) Original permittivity. (b) Reconstructed permittivity. (c) Original conductivity. (d) Reconstructed conductivity.

problems, the relative permittivities of the media are chosen higher as $\epsilon_{r2} = 4$ and $\sigma_2 = 10^{-5}$ and $\epsilon_{r3} = 4.2$ and $\sigma_3 = 10^{-4}$. Then, the relative permittivity and conductivity of all objects are chosen as $\epsilon_{obj} = 4.5$ and $\sigma_{obj} = 10^{-3}$. The reconstruction domain size is selected to be $4.5\lambda \times 2.1\lambda$. The original relative permittivity and conductivity distributions can be seen in Fig. 11(a) and Fig. 11(c) while the reconstructed relative permittivity and conductivity distributions are given in Fig. 11(b) and Fig. 11(d), respectively. Secondly, the reconstruction of 10 square objects with different dimensions and relative permittivities are addressed. The relative permittivities and conductivities of the middle and bottom spaces are $\epsilon_{r2} = 3.6$ and $\sigma_2 = 10^{-5}$ and $\epsilon_{r3} = 4$ and $\sigma_3 = 10^{-4}$. The relative permittivities of the objects are of three different values, and they can be distinguished from different colors in Fig. 12(a). These values are 4, 4.2, and 4.5, respectively. The conductivities of all objects are equal to 10^{-3} again. Fig. 12(a) and Fig. 12(b) show the original and reconstructed permittivity distributions, while the original and reconstructed conductivity distributions are given in Figs. 12(c) and 12(d).

As can be seen from all figures, the reconstructed object locations, dimensions, and shapes are very satisfactory. However, the relative permittivity values are slightly lower than they should be while the conductivity values are very close to the correct values.

4. CONCLUSION

In this study, the reconstruction of dielectric objects buried in the middle or bottom region of three-part space with locally rough interfaces is discussed. The considered inverse scattering problem is solved by distorted Born iterative method. DBIM is an iterative method for the solution of nonlinear inverse problems and requires the calculation of the background electric field and background Green's function in every iteration step. Since the background space has a complex structure both geometrically and electromagnetically, there are no analytical solutions of the background electric field and the Green's function. Here, they are calculated numerically by using the buried object approach (BOA). Several numerical analyses have been conducted to demonstrate the effectiveness of the method in the solution of the introduced problem. In numerical implementations, the effects of the medium in which the objects are buried, the geometry of the objects, and the amplitudes of the interfacial roughness on the reconstruction results are analyzed. It has been observed that the method gives very good results even if the objects are multiple or have very different geometric structures. Furthermore, the results of the reconstruction are found to be more successful if the objects are buried in the middle space than if they are buried in the bottom space. Besides, as the amplitudes of the interfacial roughnesses increase, the reconstruction results deteriorate. It should also be noted that DBIM is not very successful in the reconstruction of high-contrast objects due to the limitations of being a born approximation-based method. With the use of multiple-frequency approaches, hybrid-DBIM or modified-DBIM methods, the success of the presented work can be increased for objects with higher contrast.

APPENDIX A. CALCULATION OF THE ELECTRIC FIELD IN THREE-PART SPACE WITH PLANAR

Field u_{b0} is the field at any point of the three-part space with planar interfaces at $x_2 = d$ and $x_2 = -d$ in the case of plane wave illumination excited in top space. In other words, it is equal to the total field in three-part space illuminated by a plane wave from the top space. The corresponding geometry is shown in Fig. A1. Accordingly, this field can be expressed as follows,

$$u_{b0}(\mathbf{x}) = \begin{cases} u_i(\mathbf{x}) + u_{1r}(\mathbf{x}), & x_2 >= d \\ u_{1t}(\mathbf{x}) + u_{2r}(\mathbf{x}), & -d <= x_2 < d \\ u_{2t}(\mathbf{x}), & x_2 < -d \end{cases} \tag{A1}$$

Here, u_i is the incident field whose definition is given in (9). u_{1r} is the field reflected from $x_2 = d$ plane, and u_{1t} is the field transmitted to the second medium. This field is also the field incident to the $x_2 = -d$ interface dividing the second and third mediums. u_{2r} is the field reflected from $x_2 = -d$ plane, and u_{2t}

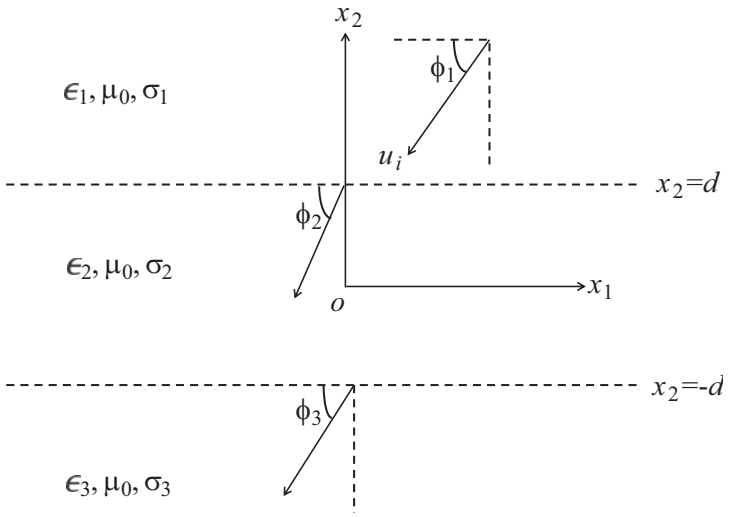

Figure A1. Three-part space with planar interface.

is the field transmitted to the third medium. Their explicit expressions are given below,

$$u_{1r}(\mathbf{x}) = R_{12}e^{-ik_1(x_1 sin\phi_1 - x_2 cos\phi_1)} \tag{A2a}$$

$$u_{1t}(\mathbf{x}) = T_{12}e^{-ik_2(x_1 sin\phi_2 + x_2 cos\phi_2)} \tag{A2b}$$

$$u_{2r}(\mathbf{x}) = T_{12}R_{23}e^{-ik_2(x_1 sin\phi_2 - x_2 cos\phi_2)} \tag{A2c}$$

$$u_{2t}(\mathbf{x}) = T_{12}T_{23}e^{-ik_3(x_1 sin\phi_3 + x_2 cos\phi_3)} \tag{A2d}$$

In Eq. (A2), R_{12}, T_{12}, R_{23}, and T_{23} are reflection and transmission coefficients between top-mid and mid-bottom media. They can be calculated by employing the boundary conditions to be provided on the interfaces,

$$R_{12} = \frac{T_{12}e^{id(k_1 cos\phi_1 - k_2 \cos\phi_2)}(1 + R_{23}) - 1}{e^{ik_1 d\cos\phi_1}} \tag{A3a}$$

$$T_{12} = \frac{2\eta_2 \sin\phi_1}{K_1 - K_2} \tag{A3b}$$

where

$$K_1 = e^{id(k_1\cos\phi_1 - k_2\cos\phi_2)}\left[1 - R_{23}\frac{\eta_1 \sin\phi_2}{\eta_2 \sin\phi_1}\right]$$

and

$$K_2 = e^{id(k_1\cos\phi_1 + k_2\cos\phi_2)}R_{23}\left[1 + \frac{\eta_1 \sin\phi_2}{\eta_2 \sin\phi_1}\right]$$

$$R_{23} = \frac{T_{23}e^{id(k_3 cos\phi_3 - k_2\cos\phi_2)} - 1}{e^{-i2dk_2\cos\phi_2}} \tag{A3c}$$

$$T_{23} = \frac{2}{\left(1 + \dfrac{\eta_2 \sin\phi_3}{\eta_3 \sin\phi_2}\right)e^{id(k_3\cos\phi_3 - k_2\cos\phi_2)}} \tag{A3d}$$

ϕ_2 and ϕ_3 shown in Eq. (A3) are obtained via Snell's law as,

$$\phi_2 = \cos^{-1}\left(\frac{k_1}{k_2}\cos\phi_1\right) \tag{A4}$$

and

$$\phi_3 = \cos^{-1}\left(\frac{k_1}{k_3}\cos\phi_1\right) \tag{A5}$$

APPENDIX B. CALCULATION OF THE GREEN'S FUNCTION OF THREE-PART SPACE WITH PLANAR INTERFACES

The Green's function of three-part space provides the following wave equation under certain boundary conditions and radiation condition,

$$\Delta G_{b0}(\mathbf{x},\mathbf{y}) + k_{b0}^2 G_{b0}(\mathbf{x},\mathbf{y}) = -\delta(\mathbf{x}-\mathbf{y}) \tag{B1}$$

Here k_{b0} is the wave number of three-part media indicated in Fig. A1, and its definition is given in Eq. (14). δ is the Dirac delta function. By solving this equation under given conditions, Green's function can be found as follows,

$$G_{b0}(\mathbf{x},\mathbf{y}) = \frac{1}{2\pi}\int_L \hat{G}_{b0}(\nu, x_2, \mathbf{y}) e^{i\nu x_1} d\nu \tag{B2}$$

where L is the horizontal integration path in regularity strip of spectral Green's function $\hat{G}_{b0}$ in complex ν plane. The spectral Green's function is

$$\hat{G}_{b0} = e^{-i\nu y_1}\begin{cases} \hat{G}_{b01}, & x_2 \geq d, y_2 \geq d \\ \hat{G}_{b02}, & d \geq x_2 \geq -d, y_2 \geq d \\ \hat{G}_{b03}, & x_2 \leq -d, y_2 \geq d \\ \hat{G}_{b04}, & x_2 \geq d, -d \leq y_2 \leq d \\ \hat{G}_{b05}, & d \geq x_2 \geq -d, -d \leq y_2 \leq d \\ \hat{G}_{b06}, & x_2 \leq -d, -d \leq y_2 \leq d \\ \hat{G}_{b07}, & x_2 \geq d, y_2 \leq d \\ \hat{G}_{b08}, & d \geq x_2 \geq -d, y_2 \leq -d \\ \hat{G}_{b09}, & x_2 \leq -d, y_2 \leq -d \end{cases} \tag{B3}$$

$$\hat{G}_{b01} = \frac{1}{2\gamma_1}\left[\frac{1+\left(\frac{\gamma_3+\gamma_2}{\gamma_3-\gamma_2}\right)e^{3\gamma_2 d}}{\left(\frac{\gamma_1-\gamma_2}{\gamma_1+\gamma_2}\right)+\left(\frac{\gamma_2+\gamma_3}{\gamma_2-\gamma_3}\right)e^{4\gamma_2 d}}\right] e^{2\gamma_1 d-\gamma_1(x_2+y_2)} + e^{-\gamma_1|x_2-y_2|} \tag{B4a}$$

$$\hat{G}_{b02} = \left[\frac{(\gamma_2-\gamma_3)+(\gamma_2+\gamma_3)e^{2\gamma_2(d-x_2)}}{(\gamma_1-\gamma_2)(\gamma_2-\gamma_3)+(\gamma_1+\gamma_2)(\gamma_2+\gamma_3)e^{4\gamma_2 d}}\right] e^{-\gamma_1 y_2-\gamma_2 x_2+d(\gamma_1+\gamma_2)} \tag{B4b}$$

$$\hat{G}_{b03} = \left[\frac{2\gamma_2 e^{(2\gamma_2+\gamma_3+\gamma_1)}}{(\gamma_1-\gamma_2)(\gamma_2-\gamma_3)+(\gamma_1+\gamma_2)(\gamma_2+\gamma_3)e^{4\gamma_2 d}}\right] e^{-\gamma_1 y_2+\gamma_3 x_2} \tag{B4c}$$

$$\hat{G}_{b04} = \left(\frac{K}{\gamma_1-\gamma_2}\right) e^{-\gamma_2 y_2+(\gamma_1+\gamma_2)d}\left[1+\frac{\gamma_2+\gamma_3}{\gamma_2-\gamma_3}e^{2\gamma_2(d+y_2)}\right] e^{-\gamma_1 x_2} \tag{B4d}$$

$$\begin{aligned}\hat{G}_{b05} = \frac{K}{2\gamma_2}\Bigg[&\left(\frac{\gamma_1+\gamma_2}{\gamma_1-\gamma_2}e^{2\gamma_2 d}-1\right)e^{-\gamma_2(x_2+y_2)} + \frac{\gamma_3+\gamma_2}{\gamma_3-\gamma_2}e^{2\gamma_2 d}e^{\gamma_2(x_2+y_2)} \\ &+\left(\frac{\gamma_1+\gamma_2}{\gamma_1-\gamma_2}\right)\left(\frac{\gamma_2+\gamma_3}{\gamma_2-\gamma_3}\right)e^{4\gamma_2 d}e^{-\gamma_2|x_2-y_2|}\Bigg]\end{aligned} \tag{B4e}$$

$$\hat{G}_{b06} = \left(\frac{K}{\gamma_3-\gamma_2}\right) e^{-\gamma_2 y_2+(\gamma_2+\gamma_3)d}\left[1+\frac{\gamma_2+\gamma_1}{\gamma_2-\gamma_1}e^{2\gamma_2(d-y_2)}\right] e^{\gamma_3 x_2} \tag{B4f}$$

$$\hat{G}_{b07} = \frac{1}{2\gamma_3}\left[\frac{1+\left(\frac{\gamma_1+\gamma_2}{\gamma_1-\gamma_2}\right)e^{3\gamma_2 d}}{\left(\frac{\gamma_3-\gamma_2}{\gamma_3+\gamma_2}\right)+\left(\frac{\gamma_2+\gamma_1}{\gamma_2-\gamma_1}\right)e^{4\gamma_2 d}}\right] e^{2\gamma_3 d+\gamma_3(x_2+y_2)} e^{-\gamma_3|x_2-y_2|} \tag{B4g}$$

$$\hat{G}_{b08} = \left[\frac{(\gamma_2-\gamma_1)+(\gamma_2+\gamma_1)e^{2\gamma_2(d+x_2)}}{(\gamma_3-\gamma_2)(\gamma_2-\gamma_1)+(\gamma_3+\gamma_2)(\gamma_2+\gamma_1)e^{4\gamma_2 d}}\right] e^{\gamma_3 y_2+\gamma_2 x_2+d(\gamma_3+\gamma_2)} \tag{B4h}$$

$$\hat{G}_{b09} = \left[\frac{2\gamma_2 e^{(2\gamma_2+\gamma_1+\gamma_3)}}{(\gamma_3-\gamma_2)(\gamma_2-\gamma_1)+(\gamma_3+\gamma_2)(\gamma_2+\gamma_1)e^{4\gamma_2 d}}\right] e^{\gamma_3 y_2-\gamma_1 x_2} \tag{B4i}$$

where γ_1, γ_2, and γ_3 are square root functions which have following definition,

$$\gamma_n = \sqrt{\nu^2 - k_n^2}, \quad n = 1, 2, 3. \tag{B5}$$

The expression of K in the above statements is as follows,

$$K = \frac{1}{1+\left(\dfrac{\gamma_1+\gamma_2}{\gamma_1-\gamma_2}\right)\left(\dfrac{\gamma_2+\gamma_3}{\gamma_2-\gamma_3}\right)e^{4\gamma_2 d}} \tag{B6}$$

REFERENCES

1. Pierri, R. and G. Leone, "Inverse scattering of dielectric cylinders by a second-order Born approximation," *IEEE Trans. Geosci. Remote Sens.*, Vol. 37, No. 1, 374–382, 1999.
2. Haddadin, O. S. and E. S. Ebbini, "Imaging strongly scattering media using a multiple frequency distorted Born iterative method," *IEEE Trans. Ultrason., Ferroelectr., Freq. Control*, Vol. 45, No. 6, 1485–1496, 1998.
3. Chew, W. C. and Y. M. Wang, "Reconstruction of two-dimensional permittivity distribution using the distorted Born iterative method," *IEEE Trans. Med. Imag.*, Vol. 9, No. 2, 218–225, 1990.
4. Zhang, L., W. Li, and F. Li, "Tomographic reconstruction using the distorted Rytov iterative method with phaseless data," *IEEE Geosci. Remote Sens. Lett.*, Vol. 5, No. 3, 479–483, 2008.
5. Chew, W. C. and Q. Liu, "Inversion of induction tool measurements using the distorted Born iterative method and CG-FFHT," *IEEE Trans. Geosci. Remote Sens.*, Vol. 32, No. 4, 878–884, 1994.
6. Zheng, H., C. Wang, and E. Li, "Modification of enhanced distorted Born iterative method for the 2D inverse problem," *IET Microw. Antenna P.*, Vol. 10, No. 10, 1036–1042, 2016.
7. Lavarello, R. and M. Oelze, "A study on the reconstruction of moderate contrast targets using the distorted Born iterative method," *IEEE Trans. Ultrason., Ferroelectr., Freq. Control*, Vol. 55, No. 1, 112–124, 2008.
8. Lavarello, R. J. and M. L. Oelze, "Tomographic reconstruction of three-dimensional volumes using the distorted Born iterative method," *IEEE Trans. Med. Imag.*, Vol. 28, No. 10, 1643–1653, 2009.
9. Hesford, A. J. and W. C. Chew, "Fast inverse scattering solutions using the distorted Born iterative method and the multilevel fast multipole algorithm," *The Journal of the Acoustical Society of America*, Vol. 128, No. 2, 679–690, 2010.
10. Cui, T. J., W. C. Chew, A. A. Aydiner, and S. Chen, "Inverse scattering of two-dimensional dielectric objects buried in a lossy earth using the distorted Born iterative method," *IEEE Trans. Geosci. Remote Sens.*, Vol. 39, No. 2, 339–346, 2001.
11. Tu, H., W. Chien, C. Chiu, and T. Hu, "Comparison of two different shape descriptions in the half-space inverse problem," *SBMO/IEEE MTT-S International Conference on Microwave and Optoelectronics*, 158–161, 2005.
12. Chiu, C. and Y. Kiang, "Electromagnetic inverse scattering of a conducting cylinder buried in a lossy half-space," *IEEE Trans. Antennas Propag.*, Vol. 40, No. 12, 1562–1565, 1992.
13. Caorsi, S., G. L. Gragnani, and M. Pastorino, "Numerical electromagnetic inverse-scattering solutions for two-dimensional infinite dielectric cylinders buried in a lossy half-space," *IEEE Trans. Microw. Theory Techn.*, Vol. 41, No. 2, 352–357, 1993.
14. Mahmoud, S. F., S. M. Ali, and J. R. Wait, "Electromagnetic scattering from a buried cylindrical inhomogeneity inside a lossy earth," *Radio Sci.*, Vol. 16, No. 6, 1285–1298, 1981.

15. Delbary, F., K. Erhard, R. Kress, R. Potthast, and J. Schulz, "Inverse electromagnetic scattering in a two-layered medium with an application to mine detection," *Inverse Probl.*, Vol. 24, No. 10, 1–26, 2008.
16. Li, F., Q. H. Liu, and L. P. Song, "Three-dimensional reconstruction of objects buried in layered media using born and distorted Born iterative methods," *IEEE Geosci. Remote Sens. Lett.*, Vol. 1, No. 2, 107–111, 2004.
17. Zhang, P., P. Fei, X. Wen, and F. Nian, "Reconstruction of objects buried in layered media based on an equivalent current source," *Progress In Electromagnetics Research M*, Vol. 44, 171–182, 2015.
18. Galdi, V., H. Feng, D. Castaon, W. C. Karl, and L. B. Felsen, "Moderately rough surface underground imaging via short-pulse quasi-ray Gaussian beams," *IEEE Trans. Antennas Propag.*, Vol. 51, No. 9, 2304–2318, 2003.
19. Firoozabadi, R., E. L. Miller, C. M. Rappaport, and A. W. Morgenthaler, "Subsurface sensing of buried objects under a randomly rough surface using scattered electromagnetic field data," *IEEE Trans. Geosci. Remote Sens.*, Vol. 45, No. 1, 104–117, 2007.
20. El-Shenawee, M., C. M. Rappaport, E. Miller, and M. Silevitch, "Three-dimensional subsurface analysis of electromagnetic scattering from penetrable/PEC objects buried under rough surfaces: Use of the steepest descent fast multipole method," *IEEE Trans. Geosci. Remote Sens.*, Vol. 39, No. 6, 1174–1182, 2001.
21. Ozdemir, O. and Y. Altuncu, "A reconstruction of dielectric objects buried under a rough surface," *13. International Workshop on Optimization and Inverse Problems in Electromagnetism*, 2014.
22. Altuncu, Y., "Reconstruction of 3D dielectric objects buried under 2D rough urfaces by using contrast source inversion method," *13. International Workshop on Optimization and Inverse Problems in Electromagnetism*, 2014.
23. Tetik, E. and I. Akduman, "3D imaging of dielectric objects buried under a rough surface by using CSI," *International Journal of Antennas and Propagation*, Vol. 2015, 1–8, 2015.
24. Hadamard, J., *Lectures on Cauchy's Problem in Linear Partial Differential Equations*, Yale University Press, New Haven, 1923.
25. Sung Chan, J. and U. Jin Choi, "Convergence analyses of the born iterative method and the distorted born iterative method," *Numerical Functional Analysis and Optimization*, Vol. 20, No. 3–4, 301–316, 2007.
26. Gilmore, C., P. Mojabi, and J. LoVetri, "Comparison of an enhanced distorted Born iterative method and the multiplicative-regularized contrast source inversion method," *IEEE Trans. Antennas Propag.*, Vol. 57, No. 8, 2341–2351, 2009.
27. Van den Berg, P. M., A. L. Van Broekhoven, and A. Abubakar, "Extended contrast source inversion, "*Inverse Probl.*, Vol. 15, 1325–1344, 1996.
28. Van den Berg, P. M. and R. E. Kleinman, "A contrast source inversion method," *Inverse Probl.*, Vol. 13, 1607–1620, 1997.
29. Abubakar, A., P. M. Van den Berg, and J. J. Mallorqui, "Imaging of biomedical data using a multiplicative regularized contrast source inversion method," *IEEE Trans. Microw. Theory Techn.*, Vol. 50, No. 7, 1761–1771, 2002.
30. Bozza, G. and M. Pastorino, "An inexact Newton-based approach to microwave imaging within the contrast source formulation," *IEEE Trans. Antennas Propag.*, Vol. 57, No. 4, 1122–1132, 2009.
31. Bloemenkamp, R. F., A. Abubakar, and P. M. Van den Berg, "Inversion of experimental multi-frequency data using the contrast source inversion method," *Inverse Probl.*, Vol. 17, 1611–1622, 2001.
32. Chen, X., "Subspace-based optimization method for solving inverse-scattering problems," *IEEE Trans. Geosci. Remote Sens.*, Vol. 48, No. 1, 42–49, 2010.
33. Ye, X. and X. Chen, "Subspace-based distorted-born iterative method for solving inverse scattering problems," *IEEE Trans. Antennas Propag.*, Vol. 65, No. 12, 7224–7232, 2017.

34. Altuncu, Y., A. Yapar, and I. Akduman, "On the scattering of electromagnetic waves by bodies buried in a half-space with locally rough interface," *IEEE Trans. Geosci. Remote Sens.*, Vol. 44, No. 6, 1435–1443, 2006.
35. Tikhonov, A. N. and V. Y. Arsenin, *Solution of Ill-posed Problems*, Winston and Sons., Washington, 1977.
36. Kirsch, A., *An Introduction to the Mathematical Theory of Inverse Problem*, Springer, New York, 1996.